

Cardiac Motion Analysis from TAG-MRI Using Radiomics

Minerva Gándara Jiménez



Universitat
Pompeu Fabra
Barcelona

CARDIAC MOTION ANALYSIS FROM TAG-MRI USING RADIOMICS

Minerva Gándara Jiménez

BACHELOR THESIS UPF / 2018

THESIS SUPERVISOR(S)

Dr. Karim Lekadir and Ms. İrem Çetin

DEPARTMENT OF INFORMATION AND COMMUNICATION TECHNOLOGIES

Acknowledgments

I would like to express my sincere gratitude to my supervisor, Karim Lekadir, for guiding and providing me with valuable help and feedback during the whole development of this final project. I have learnt a lot about the field of image processing and machine learning and I want to thank you for giving me this opportunity. I would also like to show my real appreciation to İrem Çetin, who has helped and encouraged me to do this thesis at all times. In addition, I am very grateful to Constantine Butakoff for the provided tools. Also academically, thanks to University Pompeu Fabra (UPF) for the provided knowledge during these four years, which will surely be some of the best in my life.

I wish also to reiterate my heartfelt gratitude to my family, who has supported me in the most critical moments. You have always motivated me to follow my dreams and I owe you everything. Finally, to my best friends, for your patience. Gracias.

Abstract

Abnormalities in heart wall motion are often related to cardiovascular disease (CVD), the first cause of death worldwide. In this context, tag-MRI imaging technique has the potential to become the gold-standard for quantifying regional function and therefore to enable reliable stratification of CVDs patients. However, there is a lack of comprehensive image analysis methods that can analyse the cardiac motion from tag-MRI. On the other hand, the radiomics paradigm has recently shown great promise for patient stratification in the presence of complex diseases in cardiac MRI.

In this project, the feasibility of using radiomics and machine learning for cardiac stratification in tag-MRI is investigated through a number of methods and experiments. First, a learning radiomics-based approach is implemented to predict the motion landmarks conventionally defined through semi-automatic methods, indicating limited correlations between the two types of variables. Subsequently, the potential of radiomics for cardiac motion stratification in tag-MRI is implemented based on feature selection and principal component analysis. The results obtained based on a public database of 15 tag-MRI cases show that, unlike the motion landmarks used in previous research, radiomics features estimated from tag-MRI have the potential for discriminating between distinct cardiovascular subgroups.

This thesis represents the first proof-of-concept study for deeper phenotyping and advanced stratification of cardiac motion using tag-MRI. Future work includes more extensive validation with larger clinical samples and diverse CVD subgroups.

Keywords

Cardiovascular disease, cardiac motion, tag-MRI, radiomics, machine learning, patient stratification.

Index

1. INTRODUCTION	2
1.1. Cardiovascular diseases	2
1.2. Cardiac imaging techniques for motion quantification: tag-MRI	3
1.2.1. <i>Cardiac motion assessment imaging techniques</i>	<i>3</i>
1.2.2. <i>Tag-MRI</i>	<i>4</i>
1.2.3. <i>Motion estimation techniques in tag-MRI: state-of-the-art.....</i>	<i>5</i>
1.3. Radiomics	7
1.3.1. <i>Radiomics applications in cancer quantification</i>	<i>9</i>
1.3.2. <i>Radiomics applications in non-cancer diseases.....</i>	<i>9</i>
1.4. Problem statement and specific objectives	10
2. MATERIALS AND METHODS.....	12
2.1. Dataset	12
2.1.1. <i>Tag-MRI images</i>	<i>12</i>
2.1.2. <i>Landmarks</i>	<i>13</i>
2.1.3. <i>Meshes</i>	<i>13</i>
2.2. Pre-processing.....	14
2.2.1. <i>Landmarks</i>	<i>14</i>
2.2.2. <i>Radiomics</i>	<i>17</i>
2.3. Predictive modelling of motion landmarks	20
2.3.1. <i>Input and output</i>	<i>20</i>
2.3.2. <i>Regression model.....</i>	<i>20</i>
2.3.3. <i>Validation</i>	<i>20</i>
2.4. Patient stratification using PCA.....	21
2.4.1. <i>Principal Component Analysis</i>	<i>21</i>
3. RESULTS.....	24
3.1. Link between radiomics and motion landmarks	24
3.2. Patient stratification in tag-MRI using motion landmarks	25
3.3. Patient stratification in tag-MRI using radiomics.....	27
4. DISCUSSION.....	33

List of figures

Figure 1. Cardiac images from different modalities.....	4
Figure 2. CSPAMM acquisitions	5
Figure 3. Radiomics process.....	8
Figure 4. 3DTAG images	12
Figure 5. Procrustes alignment process	14
Figure 6. Mask generation process	17
Figure 7. Pipeline of the predictive model based on radiomics.....	21
Figure 8. Landmarks movement across the cardiac cycle for male/female subjects.....	26
Figure 9. PCA plot for the 12 landmarks	27
Figure 10. Optimal radiomics for separating male vs. female dynamics	30
Figure 11. Unsuitable radiomics for discriminating male vs. female dynamics	31
Figure 12. PCA plot summarizing the 12 discriminant radiomics	32
Figure 13. Plot for two radiomics features	32

List of tables

Table 1. Classification of motion quantification methods using tag-MRI images.....	7
Table 2. Dataset description	13
Table 3. Mean errors obtained for the radiomics-based landmarks predictions.....	24
Table 4. STACOM motion challenge participants, methods and errors.	24
Table 5. Discriminant radiomics for distinguish male vs. female dynamics.....	28

1. INTRODUCTION

1.1. Cardiovascular diseases

Cardiovascular diseases (CVD) represent the first cause of death worldwide and are projected to prevail due to persistent tobacco and alcohol use, unhealthy diet, obesity and physical inactivity. Representing a total of 31% of overall deaths, approximately 17.7 million people died from CVDs in 2015, and among these 7.4 million and 8.7 million were as a result of coronary heart disease and stroke, respectively [1]. In addition, estimations suggest that 23.6 million people will die in 2030 if the current tendency remains, principally in low- and middle-income countries. Below, the most common CVDs are described:

a) Coronary Heart Diseases and Myocardial Infarction

The reduction of blood supply to coronary arteries is known as ischemia, generally caused by atherosclerosis. A complete blockage of the arteries can cause irreversible damage to the myocardial tissue which is known as myocardial infarction [2]. Over time, these abnormalities result in morphological alterations of the heart such as localized thinning of the wall and also, in some extreme case, might result in ventricular aneurysm.

b) Cardiomyopathy

Cardiomyopathies correspond to a group of diseases that specifically affect the heart muscle. They are generally divided into genetic, mixed and acquired [3]. The most common genetic cardiomyopathy is Hypertrophic Cardiomyopathy (HCM) which is a condition where myocardial wall, generally from the ventricles and septum, becomes thickened (hypertrophy). The thickened areas cause narrowing or blockage in the ventricles and make it harder for the heart to function properly [4].

The most common mixed (genetic and non-genetic) cardiomyopathy is dilated cardiomyopathy (DCM), which is characterized by ventricular chamber enlargement (dilation) and systolic dysfunction with normal left ventricle wall thickness. The causes of DCM include, infectious agents, particularly viruses, often producing myocarditis. DCM can be also caused by a number of mutations in other genes encoding cytoskeletal/sarcolemma, nuclear envelope, sarcomere, and transcriptional coactivator proteins [3].

c) Heart Failure:

Heart failure or congestive heart failure indicates a dysfunction of the heart's pumping [5]. Common causes of heart failure include coronary artery disease, such as a previous myocardial infarction, high blood pressure, atrial fibrillation and valvular heart disease.

d) Congenital Heart Disease:

Congenital heart disease is an abnormality of the structure of the heart present at birth. A variety of conditions can cause these abnormalities during embryonic development, including cardiac shunts, valve abnormalities, aortic coarctation and transposition of the great vessels [6].

1.2. Cardiac imaging techniques for motion quantification: tag-MRI

As shown by the examples of CVDs listed above, cardiac disease is often related to abnormalities in heart wall motion and cardiac dynamics. To enable early and accurate diagnosis of these CVDs, it is important that the assessment tools can objectively and accurately measure alterations in cardiac motion. In this context, cardiac imaging has played a central role for its ability to capture subtle as well as complex changes in both cardiac morphology and dynamics [7] (cf. Figure 1). This section describes some of the imaging techniques that are in use or development for cardiac motion assessment.

1.2.1. Cardiac motion assessment imaging techniques

Diverse imaging techniques have emerged for evaluating cardiac function and deformations of the heart's walls. Ultrasound-based speckle tracking is widely used due to its availability and ease of use. It is the fastest technique, but it is affected by noise and has a poor image quality. In addition, speckle tracking may simplify geometrical details and cannot be applied in distorted anatomies [8]. Computed Tomography (CT) offers a higher spatial resolution, and it is relatively inexpensive and provides fast image acquisitions. As a drawback, it is limited in clinical practice because of the radiation dose needed, especially when it involves healthy volunteers in repeated studies or patients who are likely to undergo multiple CT during live.

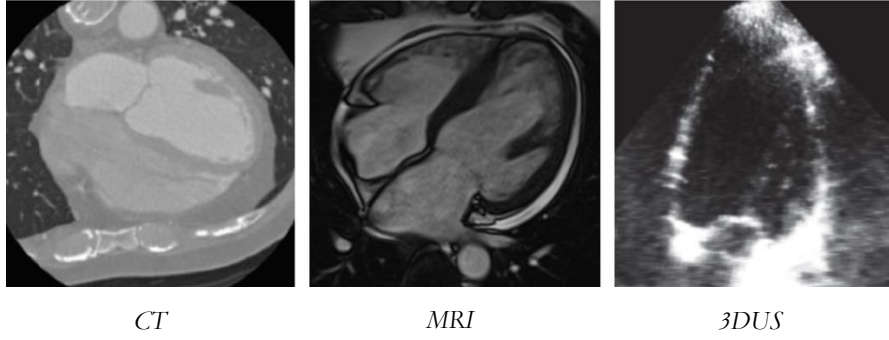


Figure 1. Cardiac images from different modalities. CT = Computed Tomography; MRI = Magnetic Resonance Imaging; 3DUS = Three-dimensional ultrasound.

In this context, cardiovascular MRI (CMR) has demonstrated to be an excellent option due to its several advantages: it is non-invasive and non-ionizing radiation, it has good spatial and temporal resolutions with 3D and 4D imaging capabilities and good soft tissue and blood pool contrast [9]. It is a modality of choice for estimating cardiac function indices such as ejection fraction and wall thickening [10]. However, conventional CMR has limitations for quantifying local motion measurements and, especially, regional myocardial deformation. This has motivated the development of specific CMR protocols, tag-MRI which is the subject of this thesis as described below

1.2.2. Tag-MRI

MRI tagging is a recognized method to evaluate and quantify regional cardiac function, especially to track local deformations (*i.e.* strain). The technique is based on creating non-invasive markers artificially placed throughout the myocardial tissue that persist during most of the cardiac cycle. By following the position of these tags, it becomes possible to estimate local myocardial deformations, including torsion.

Myocardial tissue tagging was first defined by Zerhouni *et al.* [11] and Axel *et al.* [12]. The process is based on a spatial modulation of magnetization (SPAMM) prior to image acquisition. Radiofrequency-saturation pulses separated by a wrapping gradient are used to modulate the longitudinal magnetization, producing therefore sinusoidal tag patterns or, in other words, a set of parallel stripes across the image (cf. Figure 2). The main limitation of the method is tag fading as a consequence of T_1 relaxation of the magnetization. At the end of the cardiac cycle, the tagging contrast may not be recognized impeding therefore the diastolic phases analysis.

Complementary SPAMM (CSPAMM) was later introduced by Fisher *et al.* [13]. In this case, a second set of RF-pulses and gradients is applied to the image but in the orthogonal direction, obtaining two sinusoidal patterns out of phase by 180° . This new variation is translated into a grid on the cardiac image and at each line intersection is placed a landmark or tag. These markers, as commented above, serve as a reference to track the deformations across the image frames (see Figure 2).

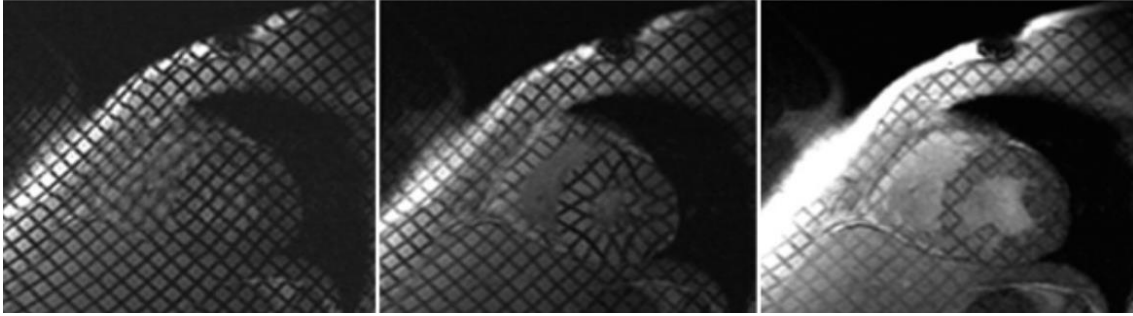


Figure 2. CSPAMM acquisitions for a healthy volunteer at 3 T. Tag features persist despite T_1 relaxation time along early systole (left), peak systole (middle) and end diastole (right) [14].

To track 3D motion in the volume of interest, commonly the left ventricle (LV), CSPAMM employs multiple sets of short-axis images (normally 6-9 images from the base to the apex) and long-axis images (normally a four-chamber plane). The right ventricle (RV) has been less studied due to its more complex geometry and motion, but we also can find some research on the topic [15], [16]. SPAMM and CSPAMM are rarely used in the clinical practice when information about specific myocardial contractility is required and not reflected in global quantitative – such as myocardial ischemia. There are also more sophisticated techniques such as strain encoding (SENC) or displacement encoding with stimulated echoes (DENSE), but they are applied principally for research purposes.

1.2.3. Motion estimation techniques in tag-MRI: state-of-the-art

MRI tagging has the potential to become the gold-standard for quantifying regional function: myocardial motion can be easily visualized, and related applications are increasing constantly. However, despite continuous improvements in the tagging protocols, tag-MRI remains a research tool mostly and new approaches are greatly needed to enable application to clinical routine [9]. There is a lack of comprehensive image analysis methods that can reliably analyse the cardiac motion from tag-MRI images. The

objective of any tagging analysis technique is to detect and track the tag features (or motion landmarks) from the tag-MRI images across the cardiac cycle. With such an approach, a contractility pattern along the heart phases can be derived for the evaluation of the heart condition [17]. Tagging analysis methods can be classified into three categories: feature-based tracking methods, frequency-based methods and tracking-based methods.

a) Feature-based methods

Feature-based methods, also called direct methods, first detect the tagging features and then track the movements accordingly. They calculate the deformation fields (or motion landmarks) directly from tagged MR images by creating or not a dense motion field from the sparse motion field by tracking the tag features. Because of the need of user-supervision to initialise the tag features using landmarks at the first frame, these methods are only semi-automatic and may not be well reproducible.

b) Frequency-based methods:

Frequency based-methods were introduced in 1999 by Osman *et al.* [18] and have become one of the most used analysis methods. They quantify the motion of tagging features from images (generally created by SPAMM) using phase information in the Fourier domain. Harmonic phase (HARP) and its enhanced versions (like 3D HARP [19] and zHARP [20]) are the main techniques used, although other methods have been developed such as Local Sine Wave Modelling (SinMod) [21] and Gabor filters [22]. The advantages of Fourier-based methods are: 1) they are automatic, without the need of extracting tag features by the user; 2) they offer more accurate results and 3) they minimize sensitivity to noise [9]. On the other hand, they can fail when the level of motion is high.

c) Tracking-based methods

These tracking-based approaches directly calculate the displacement fields by optimizing similarity transformation models between frame-to-frame intensities [23]. Spatial derivatives are further calculated to obtain strain estimations. In addition, some methods require a spatial regularization to ensure smooth results. This category consists principally of Demons-based and BSpline-based methods. They are intuitive approaches and also fast and automatic without the need of tag extraction, similarly to frequency-based

methods. The disadvantages are the long processing time and their high sensitivity to image noise and artifacts.

Table 1. Classification of motion quantification methods using tag-MRI images.

Feature-based methods	Tag beads (Amini <i>et al.</i> [24], Kerwin and Prince [25]) Tracking material markers (Sampath <i>et al.</i> [26])	
Frequency-based methods	HARP (Osman <i>et al.</i> [18]) fast-HARP (Sampath <i>et al.</i> [27]) 3D-HARP (Ryf <i>et al.</i> [19]) zHARP (Abd-Elmoniem <i>et al.</i> [20]) SinMod (Arts <i>et al.</i> [21]), Gabor filters banks (Chen <i>et al.</i> [22]), Morphon (Tautz <i>et al.</i> [28])	
Tracking-based methods	Demons-based	Optical flow (Xu <i>et al.</i> [29]) iLogDemons (Mansi <i>et al.</i> [30], McLeod <i>et al.</i> [31]) Variational non-rigid registration (Rougon <i>et al.</i> [32])
	BSpline-based	3D BSpline (Deng and Denney [33]) Non-rigid FFD registration (Chandrashekhara <i>et al.</i> [34], Shi <i>et al.</i> [35]) Volume deformable model with parameter functions (Park <i>et al.</i> [36])
	BSpline-based (spatio-temporal)	4D BSpline (Huang <i>et al.</i> [37]) 4D FFD (De Craene <i>et al.</i> [38] [39]) 4D Nurbs (Tustison and Amini [16])

As stated above, there is a great variety of motion quantification methods but they are still not used in clinical practice given the multiple disadvantages that each one presents: high computational cost, strong quality image influence, required user-supervision, etc. In most cases, the choice of the method should depend on the available tools and the specific application. It is important to note that the landmark-based methods, while popular in cardiac image analysis, have an important limitation: they only rely on a limited number of manually defined landmarks, and thus do not evaluate the entire myocardium but only a few specific locations.

1.3. Radiomics

In this thesis, we propose to investigate radiomics as an alternative method to analyse tag-MRI data and to identify differences in patient cardiac motion between subgroups; a task known as patient stratification. In other words, the aim is to differentiate patients with respect to their risk and so minimizing cost.

Radiomics is a relatively recent technique for deeper image-based phenotyping of complex diseases. It consists in the high-throughput extraction of large amounts of advanced quantitative imaging features (shape, size, boundary, texture, intensity) that result in the conversion of digital images into mineable data and the subsequent analysis for decision support [40],[41]. Radiomics have been measured from routine images such as CT, MRI or positron emission tomography (PET) images but not yet in tag-MRI.

In fact, so far, radiomics has been mostly applied in oncology to study tumour severity and treatment response. Several studies for different cancer types have shown that radiomic features provide increased predictive power when compared to conventional quantification methods (see Section 1.3.1). In addition, one advantage of radiomics is that they measure specific properties of the organs and tissues, and thus they can be interpreted easily by clinicians.

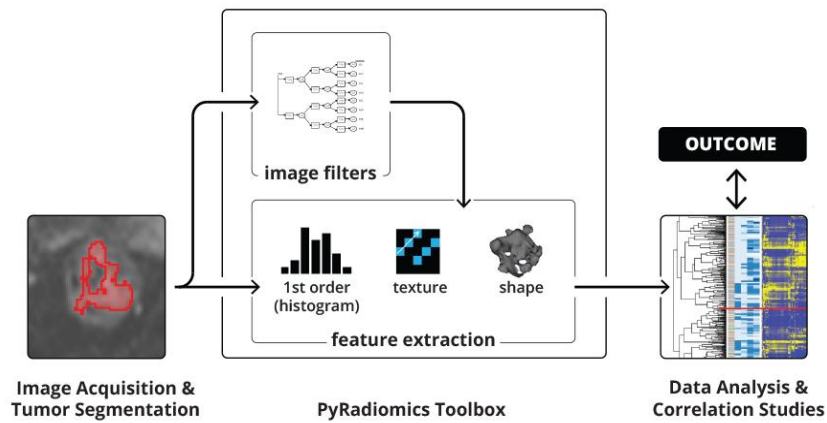


Figure 3. Radiomics process: The first steps consist of the acquisition of quality image and segmentation of the regions of interest. Then quantitative features are extracted and placed on a database which can contain clinical and genomic data. Finally, these data are processed using machine learning to develop predictive models for desired outcomes [42].

The radiomics process could be summarized in a few steps: (a) image acquisition, (b) identification of the region of interest (ROI) and segmentation, (c) possible image filtering and quantitative feature extraction, (d) mining the data to develop predictive models [40]. In this last stage, it is advisable to include patient attributes like demographic, clinical and genomic data in order to obtain clinically-meaningful predictions and thus to understand the relationships between imaging characteristics and patient information. It is important to take into consideration that semiautomatic image segmentation and filtering may be a source of variability, meaning that the whole process might not be well reproducible.

1.3.1. Radiomics applications in cancer quantification

As of June 2018, 95% of the papers indexed by Pubmed regarding radiomics (over 330), are related to cancer quantification. For example, Parmar *et al.* [43] studied how to enhance the applicability of radiomics for assessing neck and head cancer. They compared 13 feature selection methods and 11 machine-learning classification methods to predict overall survival in a cohort of 196 patients. Aerts *et al.* [44] analysed radiomics features to distinguish phenotypic differences in lung and head-and-neck cancer. They present an analysis of 440 features quantifying tumour image intensity, shape and texture extracted from CT of 1019 patients. Li, Hui *et al.* [45] assessed the role of radiomics in evaluating the risk of breast cancer recurrence. They investigated the relationships between computer-extracted breast MRI phenotypes with multigene assays. Coroller *et al.* [46] used 15 radiomics features describing stability and variance measures to show that tumours which did not respond well to neoadjuvant chemoradiation were more likely to present a rounder shape and heterogeneous appearance. Gibbs *et al.* [47] provided a method based on radiomics to discriminate between benign and malignant lesions of breast high-resolution, contrast-enhanced (CE) images. They noticed significant differences in textural features, especially using entropy and sum entropy.

1.3.2. Radiomics applications in non-cancer diseases

Some recent studies have begun to investigate the value of radiomics in other clinical domains. For instance, Sun *et al.* [48] created a classification model to diagnose Attention Deficit Hyperactivity Disorder (ADHD) based on radiomics. A total of 83 children with newly diagnosed and never-treated ADHD, as well as 87 healthy controls, participated in the study. The extracted radiomics features described shape properties of gray matter and diffusion properties of white matter and were applied in random forest classifiers. Cui *et al.* [49] proposed a radiomics-based approach to diagnose schizophrenia (SZ) based on the disrupted functional connectivity in the pathophysiology from neuroimaging. A total of 108 first-episode SZ patients and 121 healthy controls (HCs) participated in the study. An accuracy of 80% for the testing set was obtained, demonstrating that a radiomics approach can be helpful to facilitate objective SZ individualized diagnosis. Naganawa *et al.* [50] determined if texture analysis of non-contrast-enhanced CT (NECT) images is able to predict nonalcoholic steatohepatitis (NASH). They used NECT images from 88

patients who underwent a liver biopsy for the diagnosis of suspected NASH and texture feature parameters were obtained without and with filtration. The area under the receiver operating characteristic curve (AUC) of the predictive model for the validation dataset was 0.94 and the accuracy was 94%.

Finally, from Universitat Pompeu Fabra, Cetin *et al.* [51] recently presented the first radiomics approach in the field of cardiology to identify CVDs from cine-MRI and thus enable improved stratification of CVD patients. They calculated large pools of radiomics features (statistical, shape and textural features) encoding relevant changes in anatomical and image characteristics of the ventricles due to CVDs. Sequential forward feature selection was used to identify the most relevant descriptors for given CVD classes (e.g. myocardial infarction, cardiomyopathy, abnormal right ventricle). Advanced machine learning was applied to suitably integrate the selected radiomics for final multi-feature classification based on Support Vector Machines (SVMs). The authors achieved 92% classification accuracy with this radiomics-based method.

1.4. Problem statement and specific objectives

As described in this introduction, tag-MRI has the potential to become the gold-standard for cardiac motion estimation and subsequently for advanced cardiac disease quantification integrating detailed and localised analysis of the cardiac deformations. However, the modality remains far from clinical translation due to the difficulty to extract and analyse the deformation tags. Existing techniques based on the computation of motion landmarks require user interaction to define a set of initial landmarks and use a limited amount of information, typically a few landmarks, for subsequent analysis. Thus, the main goal of this thesis is to investigate the feasibility and the potential of using radiomics as a new framework for quantifying tag-MRI images and use the extraction quantitative measures as new markers for classifying patients according to their motion characteristics and deviations.

This thesis is thus structured around the following three objectives:

1. To analyse the link between radiomics and motion landmarks, to assess whether they are linked and more importantly whether the motion landmarks can be predicted from the radiomics features calculated from tag-MRI. Such predictive

models, if accurate, would enable to estimate the motion landmarks without any user interaction. However, if uncorrelated, the tag-MRI radiomics will be further investigated to assess whether they encode additional complimentary information that can improve patient stratification in CVD.

2. Subsequently, to analyse the ability of the motion landmarks as extracted from tag-MRI to identify subgroups of cardiac deformations and thus to use these for patient stratification in CVD. Because there is a lack of publicly available tag-MRI data including healthy and patients, in this thesis we will focus on analysing differences in cardiac motion between male and female subjects, which are known to have differences in their cardiac function [52].
3. Finally, to analyse the eventual added value of cardiac radiomics for cardiac motion stratification in tag-MRI, the radiomics- and landmark-based results will be compared and discussed in detail.

As such, this thesis will represent the very first attempt to use radiomics for deeper phenotyping and advanced stratification of cardiac motion using tag-MRI. The results will eventually represent a proof-of-concept of the potential of radiomics and to warrant future research in this clinical domain.

2. MATERIALS AND METHODS

2.1. Dataset

The datasets and ground truth used are publicly available via the Statistical Atlases and Computational Models of the Heart (STACOM) 2011 Challenge on cardiac motion quantification from tag-MRI. They also correspond to the data used by Tobon-Gomez *et al.* in the journal paper describing the challenge results [23]. 3D tagged magnetic resonance (tag-MRI), cine Steady State Free Precession MR (SSFP) and 3D ultrasounds (3DUS) acquisitions were provided. However, in this these only the tag-MRI images and their corresponding landmarks and meshes were utilized. The participants which volunteered to provide the imaging data consist of 15 healthy subjects without clinical history of cardiac disease (three females and 12 males, aged 28 ± 5 years). More details such as gender and body surface area are given in Table 2.

2.1.1. Tag-MRI images

Tag-MRI acquisition was carried through at the Division of Imaging Sciences and Biomedical Engineering, King's College London (IUCL), United Kingdom. It was performed using a 3T Philips Achieva System (Philips Healthcare, Best, The Netherlands). Tag-MRI datasets were acquired with three sequential breath-hold acquisitions in each orthogonal direction (TR/TE = 7.0/3.2 ms, flip angle = 19–25°, tag distance = 7 mm). Details on spatial and temporal resolution of the acquired images can be found in Table 2.

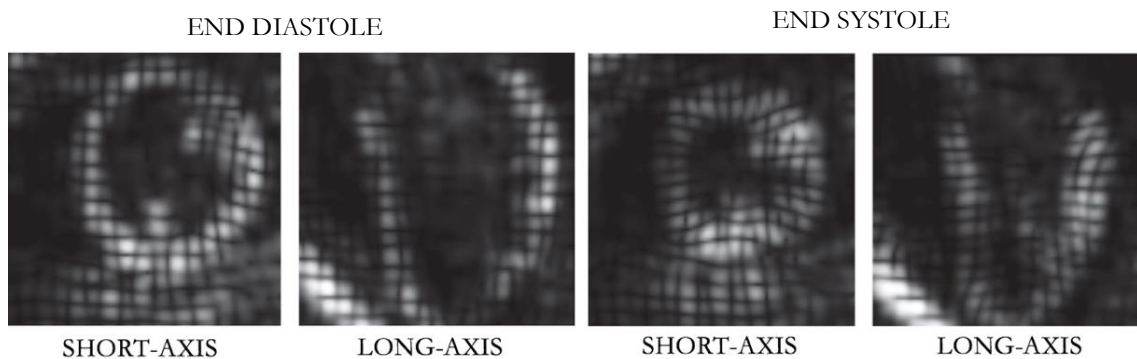


Figure 4. Tag-MRI images corresponding to end diastole and end systole cardiac phases for both short-axis and long-axis [23].

Table 2. Dataset description: SEX = sex; BSA = body surface area; SL = number of slices; PIXEL = in-plane pixel size; THK = slice thickness; PH = number of cardiac phases.

VOLUNTEER	AGE (yr)	SEX	BSA (m ²)	SL	PIXEL (mm)	THK (mm)	PH
V1	28	M	1.73	95	0.96	0.96	23
V2	30	F	1.55	80	0.96	0.96	29
V3	29	F	1.63	90	0.96	0.96	26
V4	36	M	1.84	94	0.96	0.96	23
V5	34	M	1.92	94	0.96	0.96	23
V6	32	M	1.99	100	0.96	0.96	31
V7	27	M	2.13	100	0.96	0.96	31
V8	29	M	1.78	94	0.96	0.96	30
V9	22	M	1.84	80	0.96	0.96	27
V10	22	M	1.88	100	0.96	0.96	32
V11	30	M	1.94	80	0.96	0.96	24
V12	31	M	1.78	90	0.96	0.96	38
V13	24	F	1.61	75	0.96	0.96	29
V14	20	M	1.65	90	0.96	0.96	21
V15	20	M	2.06	90	0.96	0.96	25

2.1.2. Landmarks

The process of creating ground truth landmarks was accomplished by two observers (obs1 and obs2). Each landmark was localized on the intersection point of the three orthogonal tagging planes. A total of 12 points were obtained: one per wall (anterior, lateral, posterior, septal) and per ventricular level (basal, midventricular, apical). Frame 0 was the starting point for the manual tracking: in the following frame, the observer moved the landmark to the displaced tag mark, and so on. This process was realized one landmark at a time, covering the entire cardiac cycle, guaranteeing in this way 4D tracking.

2.1.3. Meshes

In order to obtain ground truth meshes for each patient, the STACOM participants used SSFP images. Firstly, they selected the short-axis SSFP frame whose trigger time was closest to the end diastolic tag-MRI frame. After that, they manually segmented the left ventricle from this dataset by deforming a left ventricular (LV) model. Finally, using DICOM header information, they registered the resulting segmented LV mesh to the tag-MRI coordinates. These manually-segmented ground truth meshes were used in order to visualize the results of the tracking methodologies.

2.2. Pre-processing

2.2.1. Landmarks

In this project, since each patient's landmarks were placed at different positions with diverse orientations, a common reference system for all cases was essential for an accurate analysis. A Generalized Procrustes analysis (see below) was performed in this thesis to solve this misalignment problem: information about size, orientation and position was removed to focus on LV changes of shape across tag-MRI images. The landmarks corresponding to frame 0 of volunteer number 1 (V1) were chosen as the reference.

Procrustes alignment

Procrustes¹ analysis is a statistical shape analysis used to align various landmarked shapes by point correspondence (i.e. number of points which describes same anatomical positions in all shapes). Generalized Procrustes Analysis (GPA) uses isomorphic scaling, translation and rotation transformations to find the best alignment between two or more landmarked shapes. These spatial transformations, called Euclidean similarity transformations, allow to preserve the angles and parallel lines that define a shape while it is moved and scaled in order to be aligned to a target shape or other object.

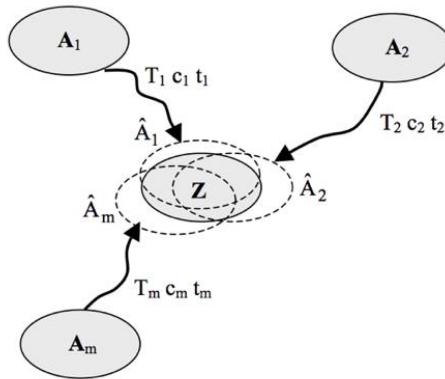


Figure 5. Procrustes alignment process. A_1 , A_2 and A_m represent the objects which have to be aligned to Z , the resulting centroid of the system. In order to obtain \hat{A}_1 , \hat{A}_2 and \hat{A}_m , it is necessary to apply the spatial transformations T_x , c_x and t_x , which correspond to the scale, rotational and translation components, respectively.

¹ Procrustes refers to a bandit in Greek's mythology. He offered accommodation to lonely travellers who became his victims: they must fit in his bed, otherwise he stretched their limbs or cut them off.

GPA is based on the following steps:

1. Choose the reference shape to which the remaining shapes will be aligned.
2. Align the shapes (or set of landmarks) to the approximate mean shape.
 - a. Calculate the centroid of each shape.
 - b. Move all shape centroid to the reference shape centroid position.
 - c. Scale each shape to mean shape size.
 - d. Rotate each shape around the reference centroid until the sum of squared distances among them is minimized.
3. Compute the new mean shape of all aligned shapes. If it remains different from the reference shape, repeat the last step (Step2).

In what follows, these spatial transformations are mathematically explained (formulas and more information from [53]).

a) Translation

Translation basically consists on moving all configurations to a reference center. The origin (0,0,0) is commonly used, but all options are equally valid. This step can be written as:

$$X_c = X_o - \frac{1}{k} \begin{pmatrix} \sum_{i=1}^k x_{i1} & \cdots & \sum_{i=1}^k x_{im} \\ \vdots & \ddots & \vdots \\ \sum_{i=1}^k x_{i1} & \cdots & \sum_{i=1}^k x_{im} \end{pmatrix} = \begin{pmatrix} x_{11} - \frac{1}{k} \sum_{i=1}^k x_{i1} & \cdots & x_{1m} - \frac{1}{k} \sum_{i=1}^k x_{im} \\ \vdots & \ddots & \vdots \\ x_{k1} - \frac{1}{k} \sum_{i=1}^k x_{i1} & \cdots & x_{km} - \frac{1}{k} \sum_{i=1}^k x_{im} \end{pmatrix}$$

where X_o is the original matrix of k -landmarks and m -dimensions ($m= 2$ or 3) and X_c corresponds to the new matrix of landmarks centered, in this case, at the origin of the reference image.

b) Isomorphic scaling

Isomorphic scaling changes the size of configuration preserving the ratio of its proportions. This transformation is used when scaling a set of shapes to a same size. In the below expression,

$$X = X_c \left(\frac{1}{\|X_c\|} \right)$$

X_c is the centered landmarks matrix and X the centered and normalized landmark matrix.

c) Rotation

Rotation is the last step of Procrustes alignment: all centered and normalized configurations are rigidly aligned to the mean form (reference shape).

X : centered and normalized landmarks matrix

Q : orthogonal rotation matrix to align X to the mean shape matrix

\bar{X} : mean shape matrix

To achieve this, this step is principally based on minimizing the difference between the mean form matrix and the rotated shape matrix resulting from the Procrustes analysis using the the sum-of-squares.

Due to the sum-of-squares of the elements of a matrix A is $\|A\| = \text{trace}(A'A)$, we have

$$\|XQ - \bar{X}\| = \text{trace}(X'X + \bar{X}'\bar{X}) - 2\text{trace}(\bar{X}'XQ),$$

expression which has to be minimized.

Interested in the part that contains Q ,

$$\text{trace}(\bar{X}'XQ) \rightarrow \max,$$

and using singular value decomposition of $\bar{X}'X = USV'$ and the cyclic property of trace

$$\text{trace}(\bar{X}'XQ) = \text{trace}(USV'Q) = \text{trace}(SV'QU) = \text{trace}(SH).$$

H results from the product of orthogonal matrices ($H = V'QU$), H is therefore an orthogonal ($p \times p$) matrix and we have that

$$\text{trace}(SH) = \sum_{i=1}^p s_i h_{ii}.$$

Since s_i are non-negative numbers and $\text{trace}(SH)$ is maximum when $h_{ii} = 1$ for $i=1,2,\dots,p$, we have: $H = I = V'QU$.

Finally, the orthogonal rotation matrix that minimizes $\|XQ - \bar{X}\|$ is $Q = VU'$ and multiplying this transformation matrix Q to X (centered and normalized matrix), the configuration X is aligned to the mean shape matrix \bar{X} .

Computation of landmark movement

Once all landmarks were placed at the same coordinate system, their pertinent movement throughout all n -frames was computed. Movement was defined as the difference between landmarks' 3D coordinates (x, y, z) at frames $i = 1, 2, 3 \dots n$ and frame 0. This way, we managed information related to landmarks' distribution change for every frame of the cardiac cycle respecting the initial condition (frame 0), instead of working directly with 3D independent coordinates.

2.2.2. Radiomics

Mask generation

In order to extract the radiomics features from the tag-MRI images, the segmentation maps or image masks corresponding to the LV myocardium are needed. The masks had to be generated at the same position and with the same orientation of all MRI images to guarantee an optimal radiomics extraction (see Figure 7). The ITK/VTK C++ library (Constantine Butakoff GitHub repository) was used for this purpose. At the end, one mask for each combination of frame mesh and tag-MRI image was obtained.

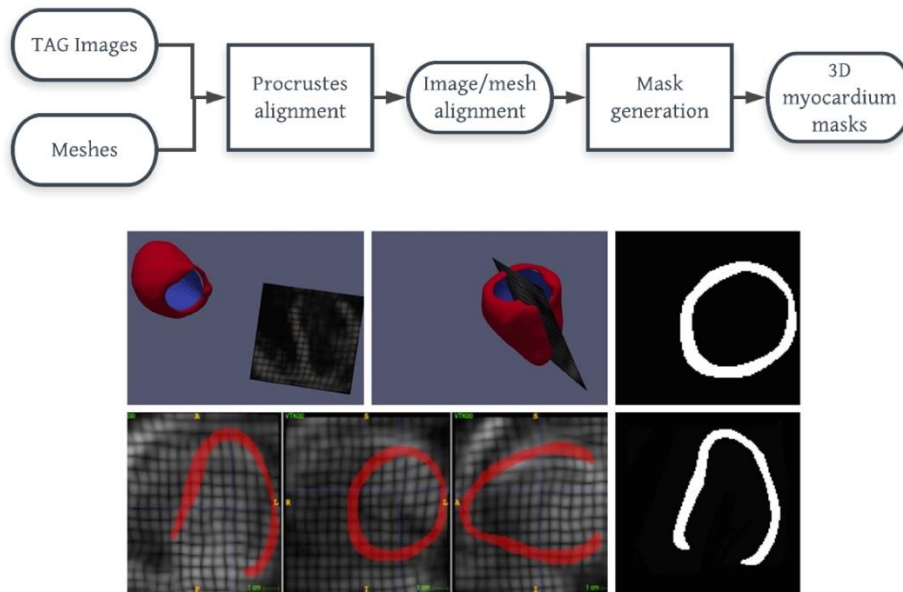


Figure 6. Mask generation process. First, Procrustes analysis is performed to the misaligned tag-image and mesh (top left). From the aligned result (top middle), 3D binary masks corresponding to the myocardium were obtained (right). It is also showed how masks were applied to tag images (bottom).

Software for radiomic estimation

We used *PyRadiomics*, an open-source platform implemented in Python which facilitates processing and extraction of radiomics features from medical images. It is based on engineered hard-coded feature algorithms and enables a flexible analysis platform and automation in data processing, feature definition and batch handling [42]. Applying this tool, three feature classes can be obtained: first-order statistics (intensity distribution) and shape-based and texture-based radiomics descriptors.

Radiomics features

From each segmented ROI in the tagged images, 106 radiomics descriptors of morphology and function of the myocardium were provided as follows:

- First order statistics descriptors included histogram-based measures, characterizing the distribution of voxel intensities without taking into account spatial relations. Some of the metrics included are mean intensities, maximum and minimum grey-level value, as well as more advanced measures such as energy, entropy and skewness. Energy, for instance, is a measure of the magnitude of voxel values in an image: larger this measure, greater the sum of squares of these values. Entropy refers mainly to uncertainty/randomness in the image value. It is a measure of the average amount of information required to encode the image values. Finally, skewness measures the asymmetry of the distribution of intensity values about the mean value.
- Shape-based features included descriptors that represent the geometrical morphology of the anatomical structure, principally size and shape (diameter, volume, area-to-volume ratio, axis, sphericity, elongation, etc.).
- Texture features are basically second and higher order imaging characteristics. They take into account changes in spatial patterns, *i.e.* they are calculated considering spatial relationships between the voxels. There are five principal subgroups [9]:
 - Gray Level Co-occurrence Matrix (GLCM). It is a square matrix with the size of the number of gray levels in the image. GLCM calculates how often a pixel with intensity value i occurs in a spatial relationship to a pixel with value j that are separated by a pixel distance $(\Delta x, \Delta y)$. Given an $M \times N$ neighbourhood of

an image containing G gray levels from 0 to $G - 1$, let $f(m, n)$ be the intensity at sample m , line n of the neighbourhood. Then,

$$P(i, j | \Delta x, \Delta y) = WQ(i, j | \Delta x, \Delta y)$$

where

$$W = \frac{1}{(M-\Delta x)(N-\Delta y)} ,$$

$$Q(i, j | \Delta x, \Delta y) = \sum_{n=1}^{N-\Delta y} \sum_{m=1}^{M-\Delta x} A$$

and

$$\begin{cases} 1 & \text{if } f(m, n) = i \text{ and } f(m + \Delta x, n + \Delta y) = j. \\ 0 & \text{elsewhere} \end{cases}$$

- Gray Level Run Length Matrix (GLRLM). It quantifies the length, in number of pixels, of consecutive pixels in a given direction that have the same gray level value. These are called gray level runs and are used to calculate metrics such as low gray level run emphasis (LGLRE) or high gray level run emphasis (HGLRE). LGLRE measures the distribution of low gray intensity values in the ROI image. A higher value indicates a greater concentration of low gray-level values, and vice versa for HGLRE.
- Gray Level Size Zone Matrix (GLSZM). This matrix quantifies how many pixels of a given gray level intensity are connected in a single group. In contrast of GLCM and GLRLM, it is rotation independent so direction is not considered. For instance, one measure that can be extracted from this matrix is gray level non-uniformity (GLN). It calculates the variability of gray-level intensity values in the ROI image. This way, a higher GLN value indicates less homogeneity in intensity values.
- Neighbouring Gray Tone Difference Matrix (NGTDM). The difference between a certain intensity value and the average gray value of its neighbours in a certain distance is calculated, supplying a local contrast measure. Contrast is considered high when an image has a large range of gray levels but also large changes between voxels and their neighbourhood. Some of the features within this category are busyness or complexity. A 'busy' image signifies that rapid changes of intensity between pixels and its neighbourhood are present so the image is non-uniform.

- Gray Level Dependence Matrix (GLDM). This matrix is a measure of coarseness. It quantifies gray level dependencies, which are defined as the quantity of connected voxels within a certain distance that are dependent on the center voxel. For instance, dependence non-uniformity (DN) measures the similarity of dependence, with a lower value indicating more homogeneity among the image.

2.3. Predictive modelling of motion landmarks

2.3.1. Input and output

Radiomics features (intensity, texture, shape and size) from tag-MRI images were used as the input of a predictive model of motion landmarks. We considered each image frame of each volunteer as one case for building the predictive model, increasing the sample size to a total of 412 (more info in Table 2). For each volunteer prediction, we used as input the radiomics descriptors at frame 0 and at the frame at which the prediction was being made (106 features + 106 features). Subsequently, the predictions of the model were landmark movement at each frame.

2.3.2. Regression model

To predict the motion landmarks, we used a machine-learning technique called Partial Least Squares (PLS) [54]. This method is based on reducing the number of predictors of X (input variable) to a smaller set of uncorrelated components. These new variables contain most of the information of X , but are also relevant for Y (output variable) as they explain as much as possible the covariance of both X and Y . This aspect differentiates PLS from Principal component analysis (PCA), which is explained in Section 2.4, as PCA only finds the components that have maximal variance in X . Once X is decomposed based on these relevant variables, least square regression is performed to predict Y . It is especially useful when the results are a set of dependent variables from a larger set of independent predictors, called multicorrelation [55].

2.3.3. Validation

To evaluate the proposed radiomics-based predictive model of the motion landmarks, we used leave-one-out cross-validation (LOOCV). As an error measure, the median Euclidean distance between the predicted movement and the real ones was computed. We

measured our results in this manner to be able to compare the accuracy of the proposed method with those obtained by the participants of the STACOM motion challenge [23]. More details are given in the results section.

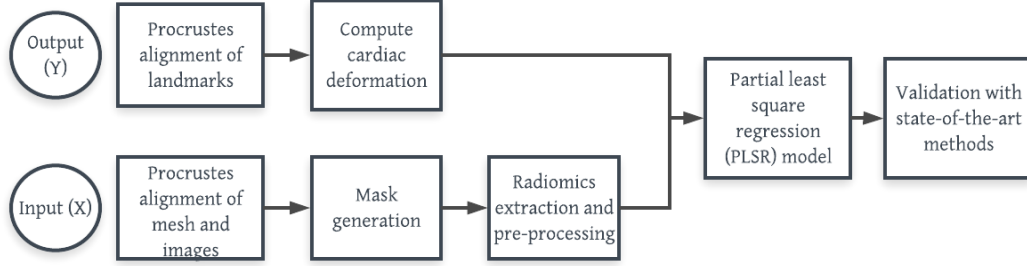


Figure 7. Pipeline of the predictive model based on radiomics.

2.4. Patient stratification using PCA

Another aim of this thesis concerns cardiac motion stratification from tag-MRI, by using and comparing the performance of motion landmarks and radiomics. As both data sit in a high dimensional space, a dimensionality reduction is required to obtain a better representation of the subgroups in a reduced space. Principal Component Analysis (PCA) was employed to achieve this.

2.4.1. Principal Component Analysis

PCA is a statistical procedure used to reduce the dimension of a large set of possible multicorrelated variables to a small set of uncorrelated values. This smaller number of linearly uncorrelated variables are called principal components, and should contain most of the information of the large set. In other words, PCA identifies the axes with a maximum variance or in which data is most spread and projects the initial feature space onto a smaller subspace. This makes data easier to visualize in order to identify patterns or highlight their similarities and differences [56]. The steps required to perform a PCA are now presented [57].

1. Compute the mean

Calculate the mean for each dimension in the d -dimensional dataset, where n is the number of the element in the set X .

$$\bar{X} = \frac{\sum_{i=1}^n X_i}{n}$$

2. Calculate covariance matrix

$$\text{cov}(X, Y) = \frac{\sum_{i=1}^n (X_i - \bar{X})(Y_i - \bar{Y})}{(n - 1)}$$

This matrix provides a measurement of the relationships between two sets of variables: if covariance takes positive values, both variables tend to show same behaviour (increase or decrease together), while the contrary case would happen if it is negative. This measure can only be computed for two-dimensional examples. In case of having, for example, a 3D data set (x, y, z) , covariance could be calculated for each pair, i.e. $\text{cov}(x, y)$, $\text{cov}(x, z)$ and $\text{cov}(y, z)$. When higher sample sizes are managed, a very useful way to keep the obtained covariance values for all dimensions is by introducing them in a matrix. This way, a covariance matrix can be written as:

$$C^{n \times n} = (c_{i,j}, c_{i,j} = \text{cov}(\text{Dim}_i, \text{Dim}_j))$$

where n is the data dimension and Dim_x is the x -th dimension.

3. Compute eigenvectors and corresponding eigenvalues

The next step is to calculate the eigenvectors and eigenvalues of the covariance matrix. Each eigenvector represents a given direction and has an associated eigenvalue, which is a number that describes how much variance exists in that direction. This way, the eigenvector with the highest eigenvalue will represent the vector in which the data are more spread out. That first eigenvector is the principal component of the data, achieving a part of the PCA's objective. The eigenvector problem can be formulated as:

$$C \cdot v = \lambda \cdot v,$$

where C is the covariance matrix, v a n -by-1 vector and λ a scalar. All λ values that satisfy the previous condition are eigenvalues of the C matrix, and v represent the eigenvectors. To find that values, we can reformulate the previous expression as:

$$\det(C - \lambda \cdot I) = 0$$

and solve to obtain the eigenvalues. Then, they are used to find the corresponding eigenvectors.

4. Sorting the eigenvectors by the descending values of the eigenvalues and choose k eigenvectors with the largest eigenvalues (for example covering a certain percentage of the total variance).

5. Transform the data onto the new space

The selected eigenvectors are then combined to form the k -dimensional eigenvector matrix, which projects the initial samples onto the smaller subspace.

3. RESULTS

3.1. Link between radiomics and motion landmarks

In this section, we first attempted to predict the motion landmarks from the radiomics variables calculated from the tag-MRI data. To this end, we built PLS regression models with the radiomics variables as input and the motion landmarks as output as described in the method section. We performed leave-one-out experiments (i.e. the subject tested was removed from the training of the PLS regression model). For each individual landmark (out of the 12 landmarks), forward sequential feature selection was performed to select a minimal set of radiomic predictors and thus to reduce overfitting.

Table 3 shows the average prediction errors (point-to-point errors) for the 12 landmarks for all cases. It can be seen that the average errors range between 1.33 mm for landmark 3 and 3.59 mm for landmark 5. In contrast, the registration-based methods used in the MICCAI challenge localized the motion landmarks with median errors of less than 1.5 mm (Table 4). This suggests that radiomics are not good predictors of the motion landmarks, speculating that even that radiomics and motion landmarks might be to some extent independent. Thus, tag-MRI radiomics may provide additional or complimentary information -in addition to the landmarks- and might be useful to improve patient stratification. This hypothesis will be tested in the next subsections.

Table 3. Mean prediction error (mm) obtained for each landmark (1-12) using the radiomics-based approach.

Radiomics approach	1	2	3	4	5	6	7	8	9	10	11	12
	2.20	2.45	1.33	3.21	3.59	3.05	2.26	2.55	2.58	2.59	1.56	1.86

Table 4. STACOM motion challenge participants, methods and errors.

Institution	Method	Error
Fraunhofer MEVIS (MEVIS), Bremen, Germany	Quadrature filter based registration (Morphon, Tautz <i>et al.</i> [28])	1.33 mm
Imperial College London – University College London (UCL), United Kingdom	Multi-image motion tracking (FFD, Shi <i>et al.</i> [35])	1.52 mm
Universitat Pompeu Fabra (UPF), Barcelona, Spain	Temporal diffeomorphic free form deformation (4D FFD, De Creane <i>et al.</i> [38] [39])	1.09 mm
Inria-Asclepios project (INRIA), France	Incompressible log-domain demons (iLogDemons, Mansi <i>et al.</i> [30] ; McLeod <i>et al.</i> [31])	1.32 mm

3.2. Patient stratification in tag-MRI using motion landmarks

In this section, we tested the ability of the motion landmarks to separate clearly distinct subgroups. Due to the limitations in our data, which correspond to a healthy population, we focused on stratification between male and female subjects. Existing research has shown that there are differences between men and women in the chamber structure and dynamics [58], [59]. Figure 9 shows the landmark changes over time, summarized using principle component analysis (PCA) over the landmark coordinates. It can be seen that none of the 12 landmarks discriminate between the male and female dynamics as captured by the landmarks. A lot of overlap can be observed in the curves of the female subjects (red color) with respect to the curves of the male subjects (blue color). Subsequently, we assessed whether combining all landmarks would lead to a better separation between the male and female groups.

To this end, we performed a PCA for all the 12 landmarks simultaneously (based on their x,y,z coordinates). Figure 10 shows that there is no clear separation between the male and female subgroups. This can mean that male and female hearts do not have different motions, which contradict existing literature [58], [59]. A more plausible explanation is related to the motion landmarks being insufficient as discriminating variables for patient stratification. Alternative variables based on radiomics will be tested in the next subsection.

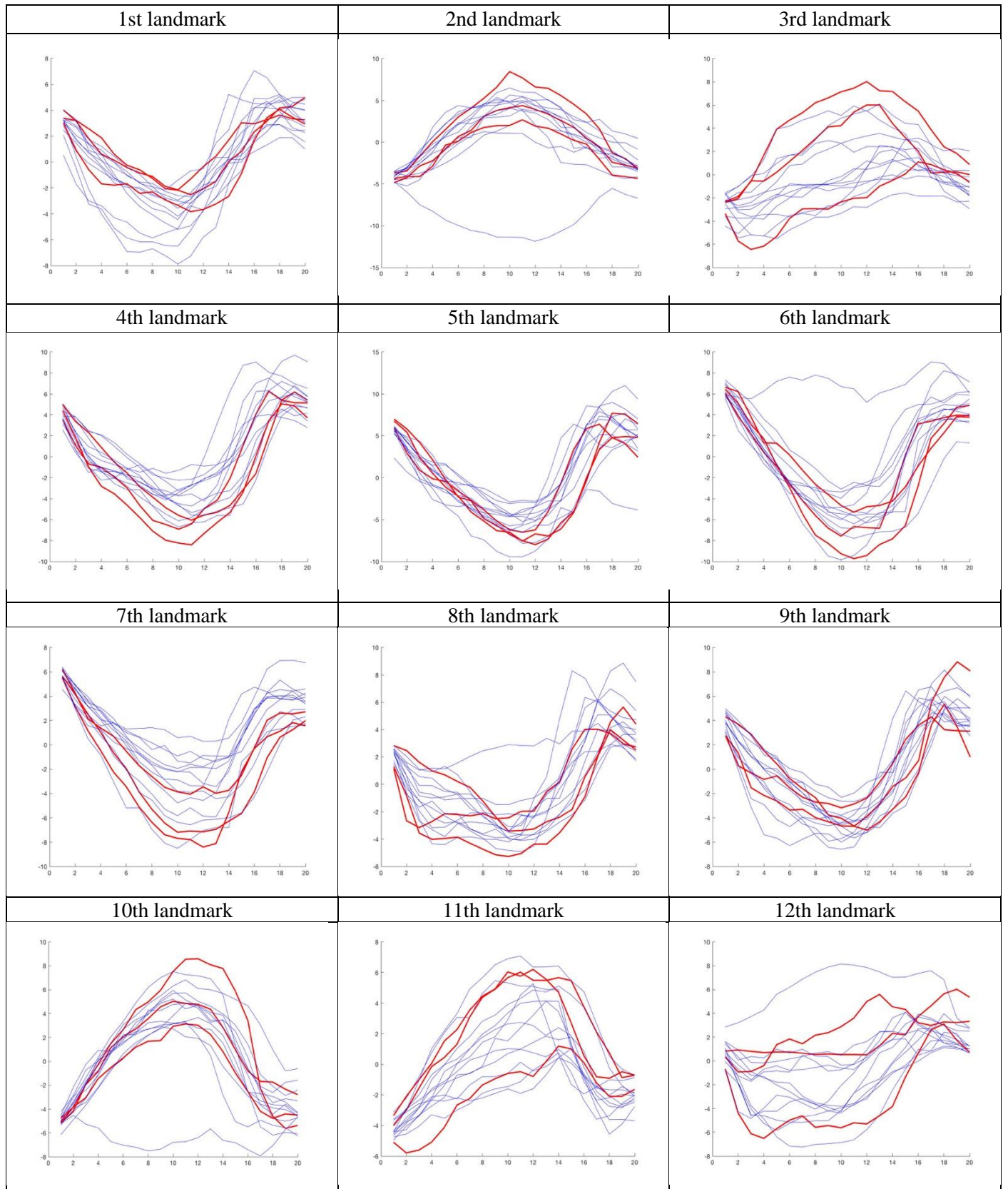


Figure 8. Landmarks movement across the cardiac cycle for male/female subjects. X-axis is expressed as number of image frames and Y-axis as distance in (mm). Male tag-MRI motion dynamics is represented in blue while female is represented in red.

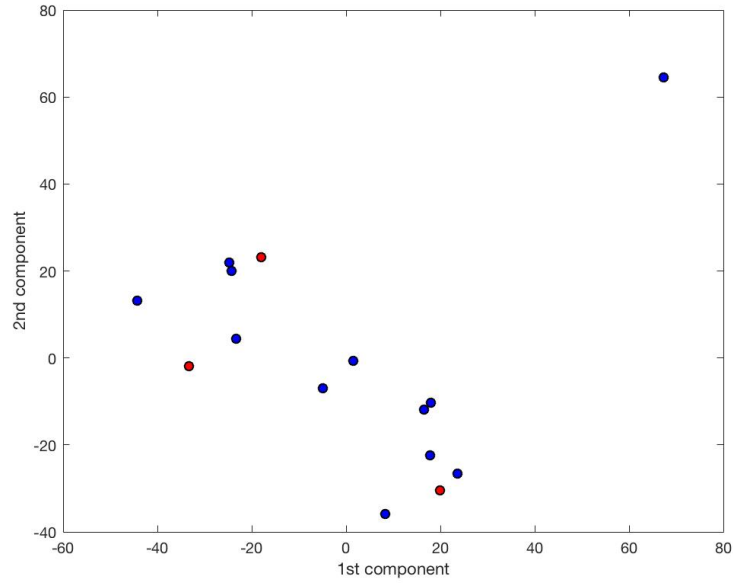


Figure 9. PCA plot for the 12 landmarks. Colour blue corresponds to male subgroup while red is referred to female cases.

3.3. Patient stratification in tag-MRI using radiomics

In this section, we assess the value of radiomics for patient stratification in tag-MRI. In a first step, we rendered the temporal radiomics curves for all 15 subjects and for all radiomics. Examples of these curves are given in Figure 11 and Figure 12. We performed a qualitative assessment of the ability of these radiomics to discriminate between male and female tag-MRI characteristics. Figure 11 shows the 12 best radiomics that were identified to separate the male and female in terms of their tag-MRI dynamics. In contrast, Figure 12 shows some examples of radiomics that are not good discriminants of the male vs. female tag MRI dynamics. The selected set of 12 radiomics are listed in the following Table 5 (definitions from *Pyradiomics* and more information also in [42]).

Table 5. Description of the radiomics useful for distinguish between male and female dynamics from tagMRI.

Name	Type	Explanation
Energy	Intensity	Energy is a measure of the magnitude of voxel values in an image.
Total energy	Intensity	Total Energy is the value of Energy feature scaled by the volume of the voxel in cubic mm.
Dependence non uniformity	Texture	Measures the similarity of dependence throughout the image, with a lower value indicating more homogeneity among dependencies in the image.
Least axis	Shape	Least axis = $4\sqrt{\lambda_{least}}$
Size zone non uniformity	Texture	Measures the variability of size zone volumes in the image, with a lower value indicating more homogeneity in size zone volumes.
Surface area	Size	Surface area is an approximation of the surface of the ROI in mm ² , calculated using a marching cubes algorithm.
Mean	Intensity	The average gray level intensity within the ROI.
Cluster prominence	Texture (GLCM)	Cluster Prominence is a measure of the skewness and asymmetry of the GLCM. A higher value implies more asymmetry around the mean while a lower value indicates a peak near the mean value and less variation about the mean
Root mean squared	Intensity	RMS is the square-root of the mean of all the squared intensity values. It is another measure of the magnitude of the image values.
90 percentile	Intensity	90 percentile
Run length non uniformity	Texture	RLN measures the similarity of run lengths throughout the image, with a lower value indicating more homogeneity among run lengths in the image.
Volume	Size	The volume of the ROI is approximated by multiplying the number of voxels in the ROI by the volume of a single voxel.

It can be seen that all radiomics types are represented in this set (shape, size, intensity and texture) but with many more intensity and texture based radiomics (9 out of 12) as these intuitively better capture the deformations of the tags over time.

Subsequently, the 12 radiomics were further reduced into two main scores using PCA. The results are shown in Figure 13, where it can be observed that the female subjects are clustered (red colour) when compared to the male subjects (blue colour). This is a clear improvement over the stratification results obtained by using the motion landmarks as previously shown in Figure 10.

Finally, to further illustrate the potential of the radiomics for patient stratification, Figure 14 shows the distribution of the 15 subjects by using as the main scores two radiomics variables only, namely one intensity (energy) and one texture (dependence non uniformity). It can be seen that these two radiomics alone enable to differentiate well the female subjects from the male subjects. This shows how a few radiomics are capable of performing motion stratification with higher accuracy than the 12 motion landmarks identified from the tags.

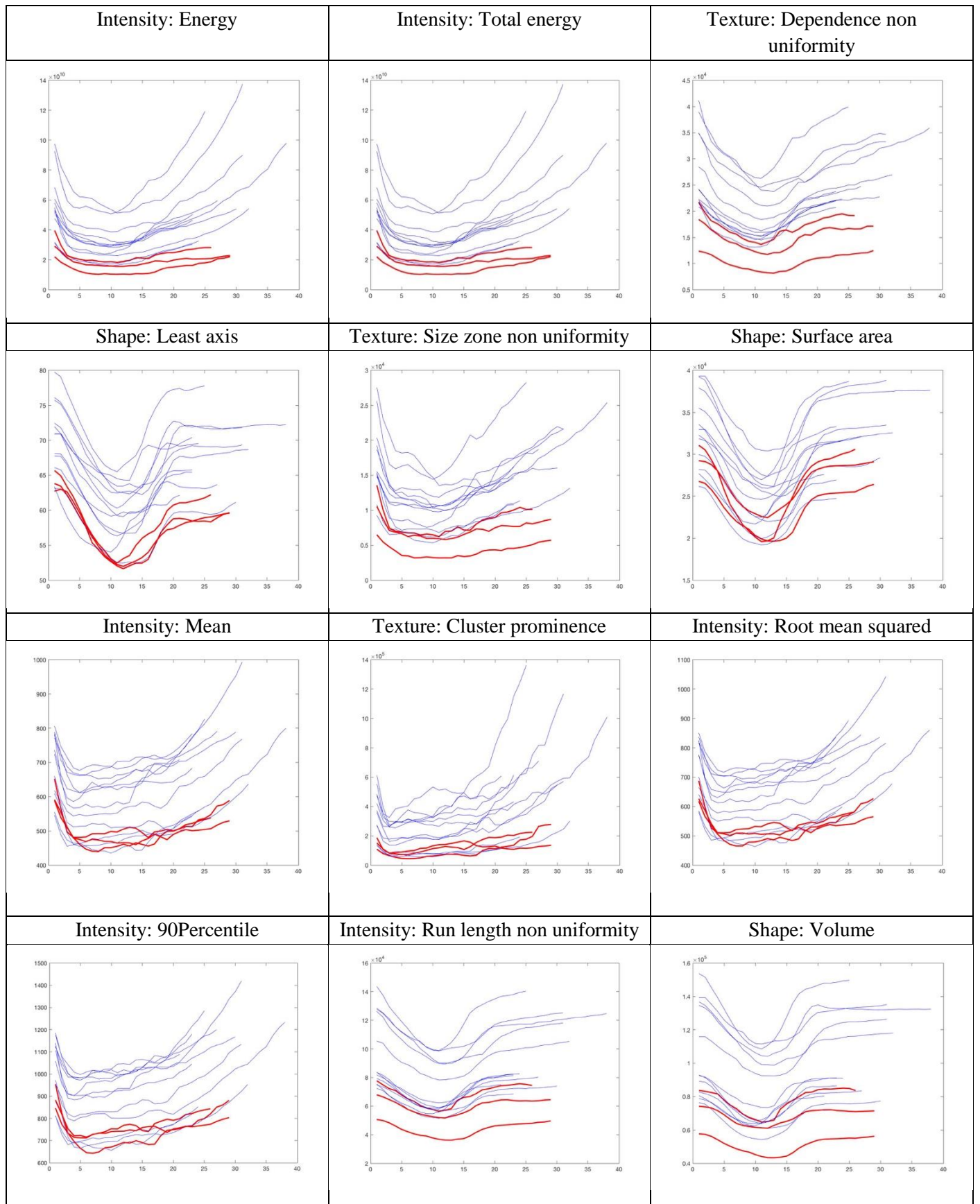


Figure 10. The best 12 discriminant radiomics features for separating male and female in terms of their tag-MRI dynamics. X-axis is expressed as number of image frames and Y-axis as feature magnitude. Male tag-MRI dynamics is represented in blue while female is represented in red.

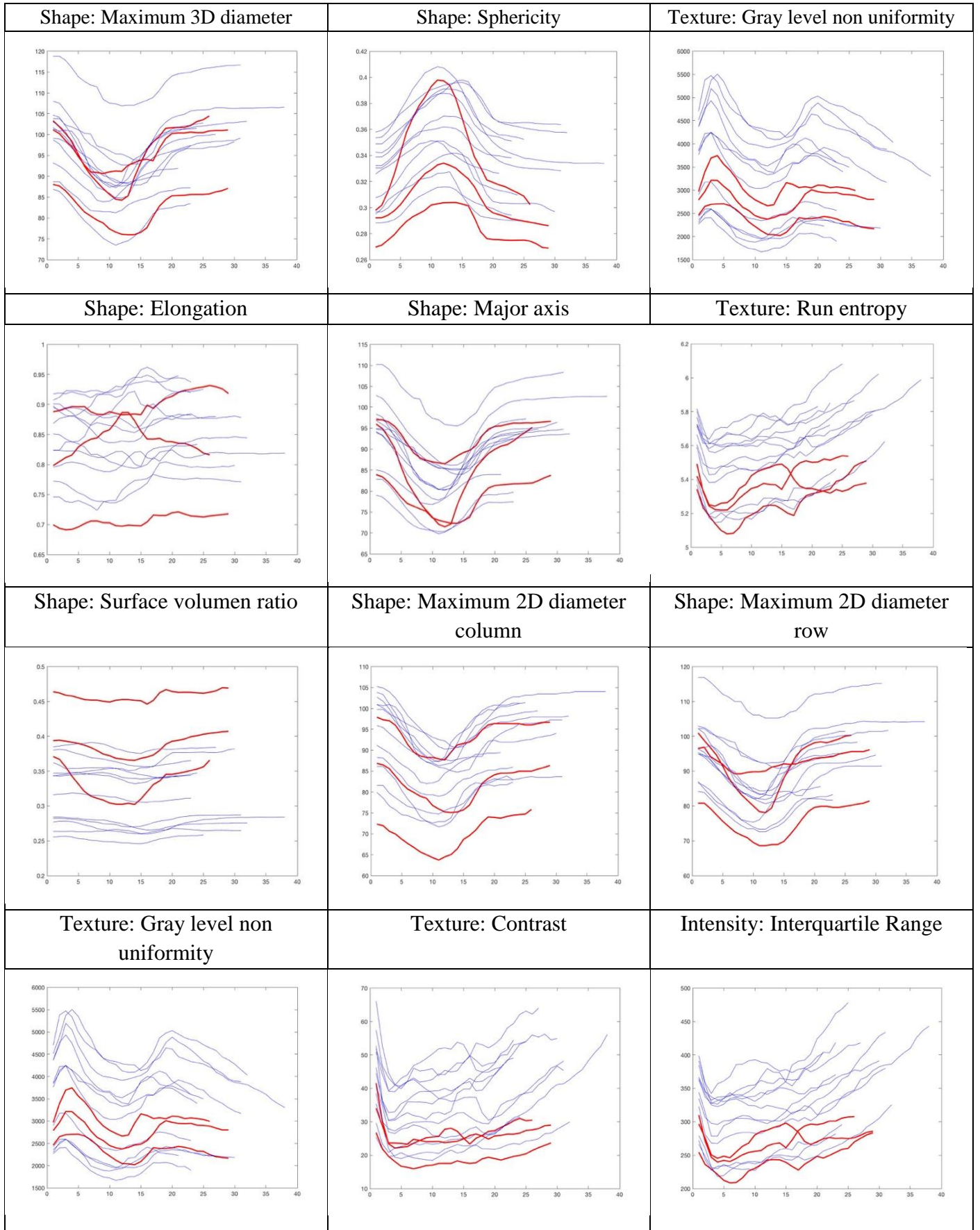


Figure 11. Unsuitable radiomics for discriminating male vs. female tag-MRI dynamics. X-axis is expressed as number of image frames and Y-axis as feature magnitude. Male tag-MRI dynamics is represented in blue while female is represented in red.

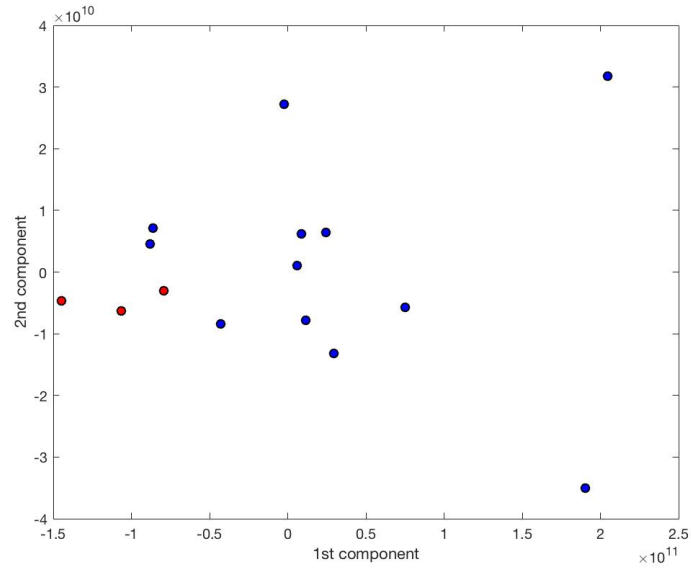


Figure 12. PCA plot summarizing the 12 discriminant radiomics. Colour blue is used to represent the male subgroup and red correspond to female subgroup.

Subsequently, the 12 radiomics were further reduced into two main scores using PCA. The results are shown in Figure 14, where it can be observed that the female subjects are clustered (red colour) when compared to the male subjects (blue colour). This is a clear improvement over the stratification results obtained by using the motion landmarks as previously shown in Figure 11.

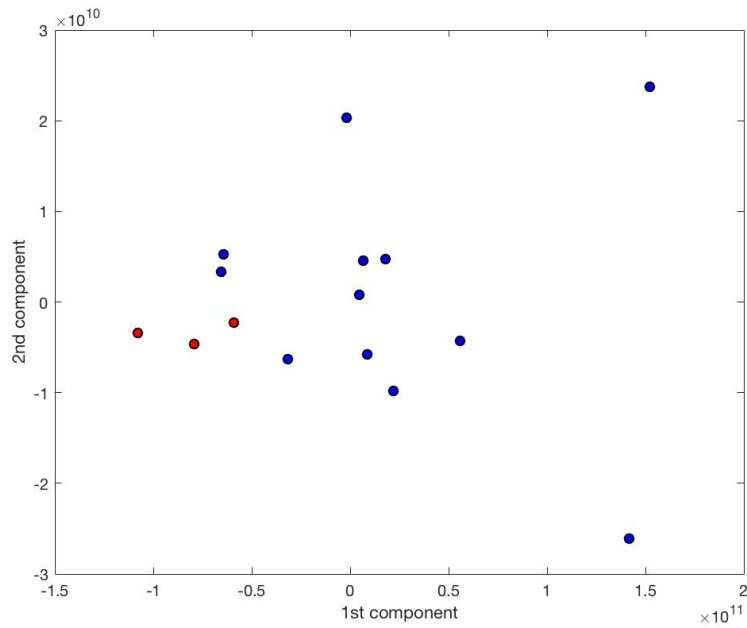


Figure 13. Plot for two radiomics features: energy (intensity) and dependence non uniformity (texture). Again, red is for female and blue for male cases.

4. DISCUSSION

In this thesis, a number of investigations were carried out with the aim to answer three main questions:

- Is it possible to predict motion landmarks from tag-MRI radiomics?
- Can motion landmarks be used to perform patient stratification, in this case for male vs. female heart comparison?
- Can radiomics improve the patient stratification achieved by the motion landmarks?

The goal of the first experiment was to test whether there is a link between radiomics features and motion landmarks extracted from tag-MRI. If such a link existed, it would become possible to build predictive models of the motion landmarks directly from the tag-MRI intensities. Existing registration-based techniques for estimating the motion landmarks require manual definition of the initial positions at frame 1 and thus a more direct method would eliminate the need for user interaction, potentially improving reproducibility. However, our results indicate that such statistical approach is less accurate than the use of existing registration-based techniques for estimating the motion landmarks. This may suggest that the radiomics features may encode distinct/complimentary information to those carried by the landmarks.

In the second experiment, we tested the value of the motion landmarks for patient stratification. For this purpose, we used the male vs. female subgroups in our datasets. However, we found that the motion landmarks do not provide a clear separation between the male and female subgroups. This suggests that the motion landmarks, while useful for assessing the heart's dynamic, seem to encode information in an incomplete manner. One of the issues is that the motion landmark is typically defined manually, which is time consuming and thus the operators often limit these landmarks to a few (12 in our dataset). This might lead to a loss of information as they do not cover all tags and all regions of the myocardium.

Finally, in the third experiment, we evaluated the potential of radiomics for patient stratification in tag-MRI as an alternative to the motion landmarks. The obtained results clearly show a greater capability for the radiomics to capture differences in cardiac

dynamics between male and female hearts. One evident advantage is that they encode information throughout the entire myocardium, while the motion landmarks only cover a few localized points. Radiomics estimate several characteristics of the tags over time, including shape and texture based. As such, they have great potential for deeper phenotyping of cardiac pathology using tag-MRI.

Limitations of the study and future perspectives. This work has some limitations that are important to mention. First of all, the sample size is relatively small to draw definitive conclusions and future work will require working with larger databases. This will be achieved by collaborating with clinical researcher at Vall d’Hebron Hospital and Queen Mary University of London. Furthermore, it would be important to test this stratification approach in more clinically meaningful dataset, to effectively look for risk stratification with pathological cases. Finally, the current study was performed mostly using qualitative evaluation. More quantitative evaluation based on larger samples would enable to study in more detail the role of each radiomic type. Nevertheless, these initial results are promising and indicate that radiomics incorporate potentially clinically useful information for disease quantification with tag-MRI. This thesis is the very first proof-of-concept performed to study the potential benefit of combining cardiac radiomics with tag-MRI to study cardiac dynamics and perform patient stratification. At the SIMBioSys research lab, where this thesis was performed, future work has been planned to extend this work, by considering larger samples and more detailed quantitative validation, but also by applying the technique to specific disease populations, such as for patients with hypertrophic cardiomyopathy or myocardial infarction. This may allow to identify more accurately and comprehensively new tag-MRI biomarkers that can be used for early diagnosis and treatment monitoring.

BIBLIOGRAPHY

- [1] W. H. Organization, “Cardiovascular diseases.” .
- [2] C. Steenbergen and N. G. Frangogiannis, “Ischemic heart disease,” in *Muscle*, vol. 1, 2012, pp. 495–521.
- [3] B. J. Maron *et al.*, “Contemporary definitions and classification of the cardiomyopathies,” *Circulation*, vol. 113, pp. 1807–1816, 2006.
- [4] B. J. Maron, “Hypertrophic Cardiomyopathy: A Systematic Review,” *Jama*, vol. 287, no. 10, pp. 1308–1320, 2002.
- [5] M. S. Figueroa, J. I. Peters, and M. Faarc, “Congestive Heart Failure: Diagnosis, Pathophysiology, Therapy, and Implications for Respiratory Care Introduction Pathophysiology of Congestive Heart Failure Evaluation of the Patient With Congestive Heart Failure Therapy for Congestive Heart Failure Pulmonary Complications of Congestive Heart Failure Exacerbations of Heart Failure: Use of CPAP and NPPV Summary.”
- [6] J. I. Hoffman and S. Kaplan, “The incidence of congenital heart disease,” *J. Am. Coll. Cardiol.*, vol. 39, no. 12, pp. 1890–1900, 2002.
- [7] T. H. Marwick and M. Schwaiger, “The future of cardiovascular imaging in the diagnosis and management of heart failure, part 1: tasks and tools,” *Circ. Cardiovasc. Imaging*, vol. 1, no. 1, pp. 58–69, Jul. 2008.
- [8] M.-Y. Jeung, P. Germain, P. Croisille, S. El, C. Roy, and A. Gangi, “CARDIAC IMAGING,” 2012.
- [9] H. Wang and A. A. Amini, “Cardiac motion and deformation recovery from MRI: A review,” *IEEE Trans. Med. Imaging*, vol. 31, no. 2, pp. 487–503, 2012.
- [10] Hui Wang and A. A. Amini, “Cardiac Motion and Deformation Recovery From MRI: A Review,” *IEEE Trans. Med. Imaging*, vol. 31, no. 2, pp. 487–503, Feb. 2012.
- [11] E. A. Zerhouni, D. M. Parish, W. J. Rogers, A. Yang, and E. P. Shapiro, “Human Heart: Tagging with MR Imaging A Method for Noninvasive Assessment of Myocardial Motion’ 59 Cardiac Radiology.”
- [12] L. Axel, A. Montillo, and D. Kim, “Tagged magnetic resonance imaging of the heart: a survey,” 2005.
- [13] Z. Qian, D. N. Metaxas, and L. Axel, “Extraction and Tracking of MRI Tagging Sheets Using a 3D Gabor Filter Bank,” in *2006 International Conference of the*

- IEEE Engineering in Medicine and Biology Society*, 2006, vol. 1, pp. 711–714.
- [14] O. Wieben, C. Francois, and S. B. Reeder, “Cardiac MRI of ischemic heart disease at 3 T: Potential and challenges,” *Eur. J. Radiol.*, vol. 65, no. 1, pp. 15–28, Jan. 2008.
 - [15] I. Haber, D. N. Metaxas, and L. Axel, “Three-dimensional motion reconstruction and analysis of the right ventricle using tagged MRI,” *Med. Image Anal.*, vol. 4, no. 4, pp. 335–55, Dec. 2000.
 - [16] N. J. Tustison and A. A. Amini, “Biventricular myocardial strains via nonrigid registration of AnFigatomical NURBS models,” *IEEE Trans. Med. Imaging*, vol. 25, no. 1, pp. 94–112, Jan. 2006.
 - [17] E.- Sayed and H. Ibrahim, “Myocardial tagging by Cardiovascular Magnetic Resonance: evolution of techniques--pulse sequences, analysis algorithms, and applications,” *J. Cardiovasc. Magn. Reson.*, vol. 13, p. 36, 2011.
 - [18] N. F. Osman, W. S. Kerwin, E. R. McVeigh, and J. L. Prince, “Cardiac motion tracking using CINE harmonic phase (HARP) magnetic resonance imaging,” *Magn. Reson. Med.*, vol. 42, no. 6, pp. 1048–60, Dec. 1999.
 - [19] S. Ryf, M. A. Spiegel, M. Gerber, and P. Boesiger, “Myocardial tagging with 3D-CSPAMM,” *J. Magn. Reson. Imaging*, vol. 16, no. 3, pp. 320–325, Sep. 2002.
 - [20] K. Z. Abd-Elmoniem, N. F. Osman, J. L. Prince, and M. Stuber, “Three-dimensional magnetic resonance myocardial motion tracking from a single image plane,” *Magn. Reson. Med.*, vol. 58, no. 1, pp. 92–102, Jul. 2007.
 - [21] T. Arts, F. W. Prinzen, T. Delhaas, J. R. Milles, A. C. Rossi, and P. Clarysse, “Mapping Displacement and Deformation of the Heart With Local Sine-Wave Modeling,” *IEEE Trans. Med. Imaging*, vol. 29, no. 5, pp. 1114–1123, May 2010.
 - [22] T. Chen and L. Axel, “Using Gabor Filter Banks and Temporal-Spatial Constraints to Compute 3D Myocardium Strain,” in *2006 International Conference of the IEEE Engineering in Medicine and Biology Society*, 2006, vol. 1, pp. 4755–4758.
 - [23] C. Tobon-Gomez *et al.*, “Benchmarking framework for myocardial tracking and deformation algorithms: An open access database,” *Med. Image Anal.*, vol. 17, no. 6, pp. 632–648, 2013.
 - [24] A. A. Amini, Y. Chen, M. Elayyadi, and P. Radeva, “Tag surface reconstruction and tracking of myocardial beads from SPAMM-MRI with parametric B-spline surfaces,” *IEEE Trans. Med. Imaging*, vol. 20, no. 2, pp. 94–103, 2001.
 - [25] W. S. Kerwin and J. L. Prince, “Generating 3-D cardiac material markers using

- tagged MRI,” 1997, pp. 313–326.
- [26] S. Sampath and J. L. Prince, “Automatic 3D tracking of cardiac material markers using slice-following and harmonic-phase MRI,” *Magn. Reson. Imaging*, vol. 25, no. 2, pp. 197–208, Feb. 2007.
 - [27] S. Sampath, J. A. Derbyshire, E. Atalar, N. F. Osman, and J. L. Prince, “Real-Time Imaging of Two-Dimensional Cardiac Strain Using a Harmonic Phase Magnetic Resonance Imaging (HARP-MRI) Pulse Sequence.”
 - [28] L. Tautz, A. Hennemuth, and H.-O. Peitgen, “Motion Analysis with Quadrature Filter Based Registration of Tagged MRI Sequences,” Springer, Berlin, Heidelberg, 2012, pp. 78–87.
 - [29] C. Xu *et al.*, “Deformation analysis of 3D tagged cardiac images using an optical flow method,” *J. Cardiovasc. Magn. Reson.*, vol. 12, no. 1, p. 19, Mar. 2010.
 - [30] T. Mansi, X. Pennec, M. Sermesant, H. Delingette, and N. Ayache, “iLogDemos: A Demons-Based Registration Algorithm for Tracking Incompressible Elastic Biological Tissues,” *Int. J. Comput. Vis.*, vol. 92, no. 1, pp. 92–111, Mar. 2011.
 - [31] K. McLeod, A. Prakosa, T. Mansi, M. Sermesant, and X. Pennec, “An Incompressible Log-Domain Demons Algorithm for Tracking Heart Tissue,” Springer, Berlin, Heidelberg, 2012, pp. 55–67.
 - [32] N. Rougon, C. Petitjean, F. Prêteux, P. Cluzel, and P. Grenier, “A non-rigid registration approach for quantifying myocardial contraction in tagged MRI using generalized information measures,” *Med. Image Anal.*, vol. 9, no. 4, pp. 353–375, Aug. 2005.
 - [33] X. Deng and T. S. Denney, “Three-Dimensional Myocardial Strain Reconstruction From Tagged MRI Using a Cylindrical B-spline Model,” *IEEE Trans. Med. Imaging*, vol. 23, no. 7, pp. 861–867, Jul. 2004.
 - [34] R. Chandrashekara, R. H. Mohiaddin, and D. Rueckert, “Analysis of 3-D Myocardial Motion in Tagged MR Images Using Nonrigid Image Registration,” *IEEE Trans. Med. Imaging*, vol. 23, no. 10, pp. 1245–1250, Oct. 2004.
 - [35] Wenzhe Shi *et al.*, “A Comprehensive Cardiac Motion Estimation Framework Using Both Untagged and 3-D Tagged MR Images Based on Nonrigid Registration,” *IEEE Trans. Med. Imaging*, vol. 31, no. 6, pp. 1263–1275, Jun. 2012.
 - [36] J. Park, D. Metaxas, and L. Axel, “Analysis of left ventricular wall motion based on volumetric deformable models and MRI-SPAMM,” *Med. Image Anal.*, vol. 1,

- no. 1, pp. 53–71, Mar. 1996.
- [37] J. Huang, D. Abendschein, V. G. Davila-Roman, and A. A. Amini, “Spatio-temporal tracking of myocardial deformations with a 4-D B-spline model from tagged MRI,” *IEEE Trans. Med. Imaging*, vol. 18, no. 10, pp. 957–972, 1999.
 - [38] M. De Craene *et al.*, “Temporal diffeomorphic free-form deformation: application to motion and strain estimation from 3D echocardiography,” *Med. Image Anal.*, vol. 16, no. 2, pp. 427–50, Feb. 2012.
 - [39] M. De Craene *et al.*, “Temporal Diffeomorphic Free Form Deformation (TDFFD) Applied to Motion and Deformation Quantification of Tagged MRI Sequences,” Springer, Berlin, Heidelberg, 2012, pp. 68–77.
 - [40] R. J. Gillies, P. E. Kinahan, and H. Hricak, “Radiomics: Images Are More than Pictures, They Are Data,” *Radiology*, vol. 278, no. 2, pp. 563–577, 2016.
 - [41] M. Avanzo, J. Stancanello, and I. El Naqa, “Beyond imaging: The promise of radiomics,” *Phys. Medica*, vol. 38, pp. 122–139, Jun. 2017.
 - [42] J. J. M. van Griethuysen *et al.*, “Computational Radiomics System to Decode the Radiographic Phenotype,” *Cancer Res.*, vol. 77, no. 21, pp. e104–e107, Nov. 2017.
 - [43] C. Parmar, P. Grossmann, D. Rietveld, M. M. Rietbergen, P. Lambin, and H. J. W. L. Aerts, “Radiomic Machine-Learning Classifiers for Prognostic Biomarkers of Head and Neck Cancer,” *Front. Oncol.*, vol. 5, p. 272, Dec. 2015.
 - [44] H. J. W. L. Aerts *et al.*, “Decoding tumour phenotype by noninvasive imaging using a quantitative radiomics approach,” *Nat. Commun.*, vol. 5, p. 4006, Jun. 2014.
 - [45] H. Li *et al.*, “MR Imaging Radiomics Signatures for Predicting the Risk of Breast Cancer Recurrence as Given by Research Versions of MammaPrint, Oncotype DX, and PAM50 Gene Assays,” *Radiology*, vol. 281, no. 2, pp. 382–391, Nov. 2016.
 - [46] T. P. Coroller *et al.*, “Radiomic phenotype features predict pathological response in non-small cell lung cancer,” *Radiother. Oncol.*, vol. 119, no. 3, pp. 480–6, Jun. 2016.
 - [47] P. Gibbs and L. W. Turnbull, “Textural analysis of contrast-enhanced MR images of the breast,” *Magn. Reson. Med.*, vol. 50, no. 1, pp. 92–98, Jul. 2003.
 - [48] H. Sun *et al.*, “Psychoradiologic Utility of MR Imaging for Diagnosis of Attention Deficit Hyperactivity Disorder: A Radiomics Analysis,” *Radiology*, vol. 287, no. 2, pp. 620–630, May 2018.

- [49] L.-B. Cui *et al.*, “Disease Definition for Schizophrenia by Functional Connectivity Using Radiomics Strategy,” *Schizophr. Bull.*, Feb. 2018.
- [50] S. Naganawa *et al.*, “Imaging prediction of nonalcoholic steatohepatitis using computed tomography texture analysis,” *Eur. Radiol.*, Feb. 2018.
- [51] I. Cetin *et al.*, “A Radiomics Approach to Computer-Aided Diagnosis with Cardiac Cine-MRI.”
- [52] F. Kolar and B. Ostadal, “Sex differences in cardiovascular function,” *Acta Physiol.*, vol. 207, no. 4, pp. 584–587, Apr. 2013.
- [53] A. Ross, “Procrustes Analysis.”
- [54] I. Helland, “Partial Least Squares Regression,” in *Wiley StatsRef: Statistics Reference Online*, Chichester, UK: John Wiley & Sons, Ltd, 2014.
- [55] H. Abdi, “Partial Least Squares (PLS) Regression.”
- [56] Sebastian Raschka, “Implementing a Principal Component Analysis (PCA),” 2014. [Online]. Available: http://sebastianraschka.com/Articles/2014_pca_step_by_step.html#class-attributes-of-pca. [Accessed: 26-May-2018].
- [57] L. I. Smith, “A tutorial on Principal Components Analysis,” 2002.
- [58] C. S. Hayward, W. V Kalnins, and R. P. Kelly, “Gender-related differences in left ventricular chamber function.,” *Cardiovasc. Res.*, vol. 49, no. 2, pp. 340–50, Feb. 2001.
- [59] J. Sandstede *et al.*, “Age- and gender-specific differences in left and right ventricular cardiac function and mass determined by cine magnetic resonance imaging,” *Eur. Radiol.*, vol. 10, no. 3, pp. 438–442, Feb. 2000.